![HAL open science logo]

Acoustical characterisation and monitoring of microbubble clouds

Lilian d'Hondt, Matthieu Cavaro, Cédric Payan, Serge Mensah

▶ **To cite this version:**

Accepted Manuscript

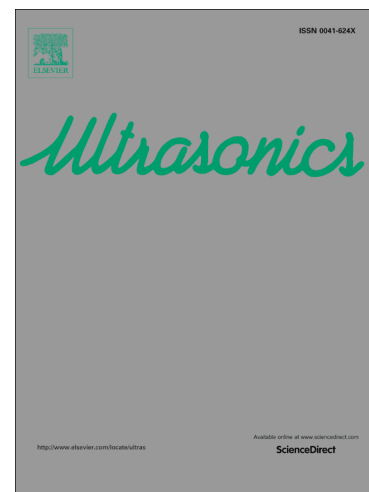Acoustical characterisation and monitoring of microbubble clouds

Lilian D'Hondt, Matthieu Cavaro, Cédric Payan, Serge Mensah

Please cite this article as: L. D'Hondt, M. Cavaro, C. Payan, S. Mensah, Acoustical characterisation and monitoring of microbubble clouds, *Ultrasonics* (2019), doi: https://doi.org/10.1016/j.ultras.2019.03.009

Acoustical characterisation and monitoring of microbubble clouds

Lilian D'Hondt[†,††], Matthieu Cavaro[†], Cédric Payan[††] and Serge Mensah[††]

[†] CEA – DEN/CAD/DTN/STCP/LISM – Bat 202 – 13108 St-Paul-lez-Durance - France

[††] Aix-Marseille Univ, CNRS, Centrale Marseille, LMA, Marseille, France

Contact: dhondt.lilian@gmail.com; matthieu.cavaro@cea.fr

Argon microbubbles will exist in the primary sodium of the next generation of sodium-cooled fast reactors (SFR). Due to its opacity, acoustic methods will be used for the in-service inspection in these reactors, but the presence of such bubbles will greatly affect ultrasonic wave propagation. Moreover, these bubbles can lead to the formation of gas pockets in the reactor and impact cavitation and boiling phenomena. It is therefore necessary to characterise what is called the 'microbubble cloud' by providing the volume fraction and the bubble size distribution. Safety requirements in this field call for robust inspection methods based on very few assumptions about the bubble populations. The objective of this study is to assess the performance of spectroscopic methods in the presence of bubbles with high polydispersity and to monitor an evolving cloud of microbubbles. The histogram and void fractions were estimated according to the regularised inversion of the complex wave number's integral equation. To reduce the need for prior information on the bubble cloud, a specific procedure was used to estimate the maximum radius of the population. The results are presented on the basis of the experimental data obtained and then compared with optical measurements.

1 INTRODUCTION

There will be a normal, continuous microbubble cloud in the primary system of the Generation IV sodium-cooled fast reactor (SFR) prototype called ASTRID[1], due to the existence of the argon gas plenum. Although there is no direct characterisation of the bubble cloud in SFRs, indirect measurements and existing calculation codes, such as VIBUL [1] - developed in the 90s at the CEA - give bubble sizes ranging from a few µm to a few tens of µm for a void fraction about 10^{-6} . As sodium is an opaque liquid metal, visual inspection of the reactor is impossible. Consequently, ultrasonic inspection methods are preferred, for example, to check the presence and position of some components such as fuel sub-assemblies, or to monitor the structural health of components (SHM). For this purpose, the telemetric approaches generally used may be severely altered if the speed of sound of the bubbly mixture is modified by the presence of bubbles in the sodium. Moreover, microbubbles have an impact on cavitation and boiling, acting as germs which could also lead to the formation of gas pockets in the reactor. For these reasons, safety requires the characterisation of this microbubble cloud using as few assumptions as possible [2].

In this paper, the term 'characterisation' refers to the estimation of the void fraction $\tau = volume_{gas}/volume_{total}$ and the bubble radius distribution. Interest in bubbly liquid characterisation is not new; Medwin [3], [4] covered this issue in 1970 when analysing the bubble population on top of oceans. An analytic expression was used to estimate the bubble radius distribution from attenuation measurements. Only the resonant bubbles were taken into account. This method has since been improved by Caruthers and Elmore [5], [6] who implemented an iterative procedure to overcome the approximations made by Medwin. Commander and Moritz [7] then showed that the non-resonant bubbles also needed to be taken into account to produce more reliable results. This implies the use of numerical methods to solve the integral equation that links the bubble distribution to their acoustic properties. The first numeric approach was proposed by Commander and Moritz [8] and was later improved by the Dynaflow laboratory. Duraiswami *et al.* [9]–[13] considered the contribution of velocity measurements in the inversion process. Leighton [14] suggested the use the "L-curve" method to determine the regularisation parameter used to optimise the inversion process.

However, the radius range was always fixed prior to the measurements in all the papers listed above. This is in contradiction with an 'assumption-free approach'. Moreover, the bubble size histograms given in the literature have poor resolution (bin size $\approx 10\ \mu m$) and the void fractions are generally not estimated. Furthermore, the results are not systematically compared against alternative measurements.

This paper describes a method that is able to continuously monitor the microbubble cloud in operational SFR conditions. It is based on the spectroscopic measurement of attenuation and sound speed with no prior information about the

---

[1] Advanced Sodium Technological Reactor for Industrial Demonstration

bubble size interval to obtain the void fraction and bubble size distribution. The experimental acoustic results of this method have been compared with optical measurements, thus providing both the bubble size distribution and void fraction.

The theoretical background is presented in the first section. The inversion procedure is then detailed and validated against two kinds of bubble distributions. Next, the experimental bench designed to reproduce - in water – the SFR operational conditions is described. Finally, the method is validated experimentally for a stationary distribution and for the continuous monitoring of a varying bubble cloud.

2   THEORETICAL BACKGROUND

The propagation of a pressure wave in a bubbly liquid can be described by the wave equation derived by Commander and Prosperetti [15]. This equation, deduced from the linearisation of the Keller-Miksis equation leads to the expression of the wave number $\underline{k}_m$:

$$\frac{\underline{k}_m^2}{} = \frac{\omega^2}{c_{liq}^2} + 4\pi\omega^2 \int_0^\infty \frac{aN(a)}{\omega_0^2 - \omega^2 + 2i\beta\omega} \, da \qquad (1)$$

where ω is the wave's pulsation; c_{liq} is the sound speed in pure water (without bubbles); $N(a)$ is the number of bubbles per unit volume with a radius between a and $a + da$; ω_0 is the resonance pulsation of a bubble with a radius a, and β is the damping coefficient associated with the thermal, viscous and radiative processes.

The sound speed V_m and attenuation A_m of the effective medium can be calculated on the basis of Eq. (1). Let u and v be the dimensionless velocity and attenuation coefficients:

$$\begin{cases} u = Im\big(\underline{k}_m/k_{liq}\big) \\ v = -Re\big(\underline{k}_m/k_{liq}\big) \end{cases} \qquad (2)$$

where k_{liq} is the wave number in pure liquid. Then:

$$\begin{cases} V_m = c_{liq}/u \\ A_m = 20\log(e)\,(\omega v/c_{liq}) \end{cases} \qquad (3)$$
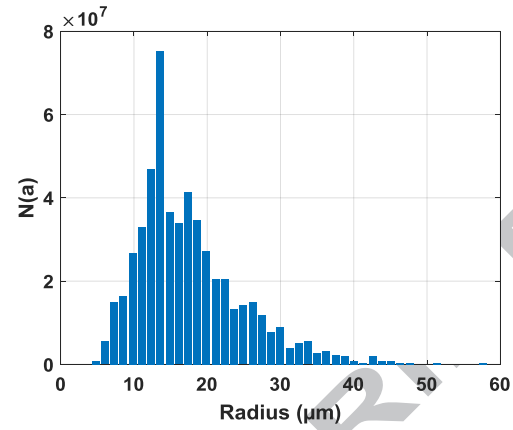

Figure 1: Experimental distribution. Void fraction: $\tau = 1.9 * 10^{-5}$

An experimental distribution was used in this section to describe the concepts and the method (Figure 1). This distribution was obtained using the optical image processing described in Section 3.2.3.

Using equation (3), the dispersion curves corresponding to this bubble size distribution have been plotted in Figure 2.
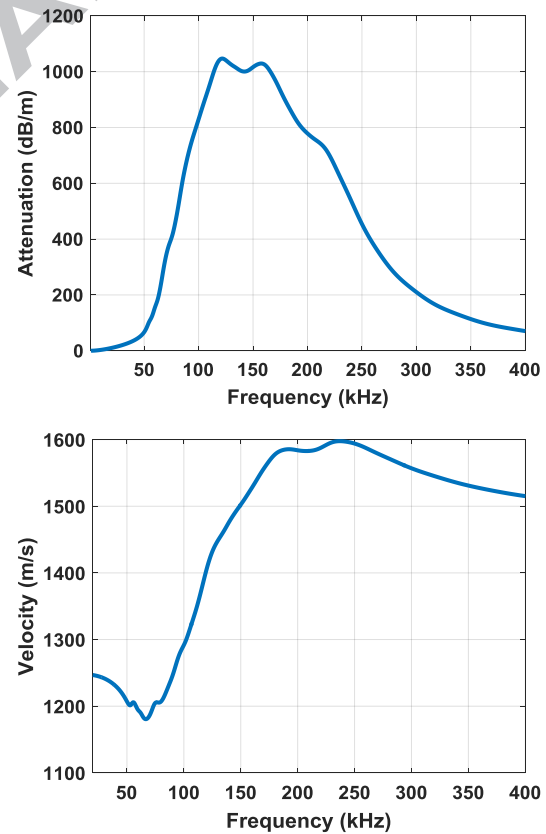

Figure 2: Dispersion curves calculated using Eq. (3)

Determining the characteristics of the bubble cloud from spectral measurements implies an inversion of Eq. (1). By separating the complex wave number into real and imaginary parts, Fredholm equations of the first kind can be derived [11], which leads to:

$$\begin{cases} u^2 - v^2 - 1 = \int_0^\infty k_1(\omega,a)N(a)da \\ uv = \int_0^\infty k_2(\omega,a)N(a)da \end{cases} \quad (4)$$

where $N(a)$ is the bubble size distribution. The expressions of the kernels $k_i(\omega,a)$ are as follows:

$$\begin{cases} k_1(\omega,a) = \dfrac{(\omega_0^2 - \omega^2)a}{(\omega_0^2 - \omega^2)^2 + 4\beta^2\omega^2} \\ k_2(\omega,a) = \dfrac{\beta\omega a}{(\omega_0^2 - \omega^2)^2 + 4\beta^2\omega^2} \end{cases} \quad (5)$$

According to Duraiswami [11], the k_2-based expression provides more robust estimations. In all cases, we need to invert an equation of the form:

$$\xi(\omega) = \int_0^{a_{max}} k(\omega,a)N(a)da \quad (6)$$

where a_{max} is greater than the bubble cloud's maximum radius. This equation discretises into:

$$\Xi = KN \quad (7)$$

where $\Xi_i = \xi(\omega_i)$, $N_i \equiv N(a_i)$ and K an $m \times n$ matrix whose coefficients are:

$$K_{ij} = \int_{a_{j-1}}^{a_{j+1}} k(\omega_i,a)B_j(a)da \quad (8)$$

B_j is the jth linear B-spline [16]. The number of measurements m is equal to n, the number of radius classes of the bubble size histogram.

As problem (7) is ill-conditioned, a Tikhonov regularisation procedure was introduced [17], [18] and led to the solution:

$$N_\lambda = \arg\min \left\| \begin{pmatrix} KN \\ \lambda L \end{pmatrix} - \begin{pmatrix} \Xi \\ \lambda L N_0 \end{pmatrix} \right\|_2 \quad (9)$$

Under the positive and finiteness constraints:

$$\begin{cases} \forall i \;\; N_i \geq 0 \\ \tau = \dfrac{4}{3}\pi \sum_i a_i^3 N_i \leq 1 \end{cases} \quad (10)$$

λ is the regularisation parameter. It must be correctly adjusted and L is a tridiagonal matrix: $L = \text{tridiag}(1,-2,1)$. N_0 is an *a priori* estimation of the solution N that can be set to zero if no information is available. Here, $N_0 \equiv 0$. This equation can be solved using a least-square algorithm. Moreover, if the void fraction can be estimated separately, for example through Wood's model using low-frequency acoustic velocity measurements [19], this value can be introduced into the set of constraints.
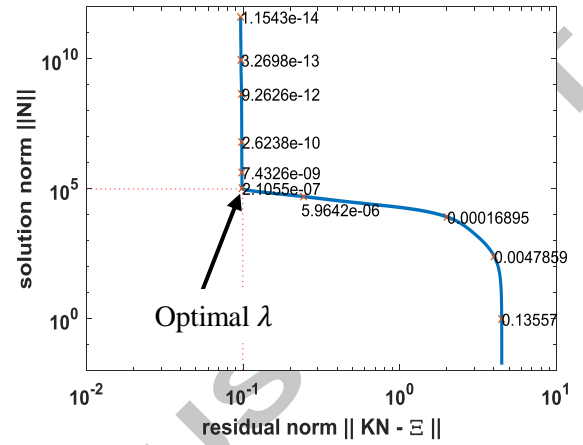

Figure 3: Typical L-curve obtained using the scripts by Hansen [18]

In order to obtain a good estimation N_λ of the bubble size distributions, the regularisation parameter was adjusted using the L-curve method described by Hansen [17]. The L-curve plots $\|N\|_2$ versus the residual norm $\|KN_\lambda - \Xi\|_2$ at different λ. On the one hand, if the regularisation parameter is too small, the residual norm is reduced, but the solution norm may still be large since the problem is ill-conditioned. On the other hand, if the regularisation is significant, the solution is dominated by regularisation errors. Hansen has shown, with respect to the so-called Discrete Picard Condition, that a physical approximation of N exists. In this case, the L-curve is indeed "L-shaped" and the optimal regularisation parameter lies at its corner (Figure 3).

3 MATERIALS AND METHOD

3.1 Determining the maximum radius of integration

Intuitively, the maximum radius of integration a_{max} (Eq. (6)) should be greater than the radius of the largest bubble in the cloud. However, it should not be too large to avoid unnecessary classes. In order to determine a_{max}, a "L-surface" was built to correspond to the surface spanned by the L-curves when the maximum radius varies (Figure 4).
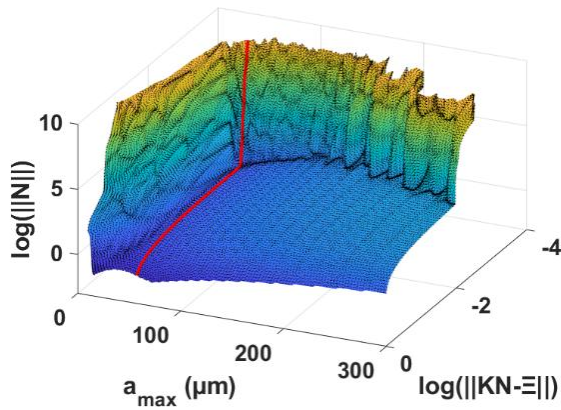
Figure 4: L-surface for an experimental bubble size distribution. The red line plots the L-curve with the selected a_{max}.

When $a_{max} < \arg\max[N \neq \{0\}]$, the radius range is incoherent with the dispersion curves, the L-curves therefore are not clearly L-shaped and they do not provide a strong curvature (at the corner) as a function of λ. Conversely, when $a_{max} \rightarrow +\infty$, the radius histogram will have excessively larges classes and the solution will be 'blurred'. The optimal maximum radius is then the smallest of those providing a sharp L-curve with an almost constant solution norm for large λ. Equation (9) was then solved using the regularisation parameter proposed by this L-curve.
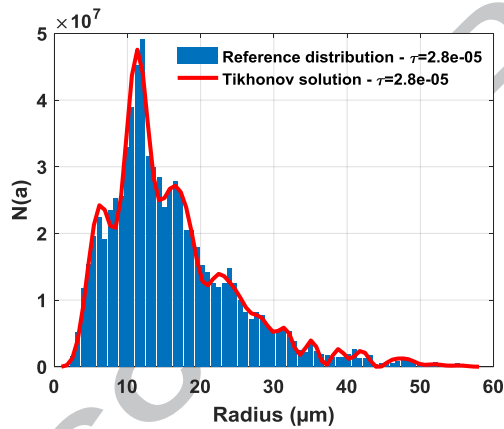

Figure 5: A reference distribution obtained optically (blue bars) and the recovered solution (red line) using eq. (9)

This has been simulated based on an optically characterised experimental distribution (Figure 1). The L-surface provided a good estimation of the bubble cloud's maximum radius. The proposed maximum radius is $58~\mu m$, which is in agreement with the distribution. Based on the optical data, acoustic dispersion curves were assessed using Eq. (3) and a small amount of Gaussian noise was added (3%) to the measurement vector Ξ to mimic experimental noise. The result of the inversion is shown in Figure 5.
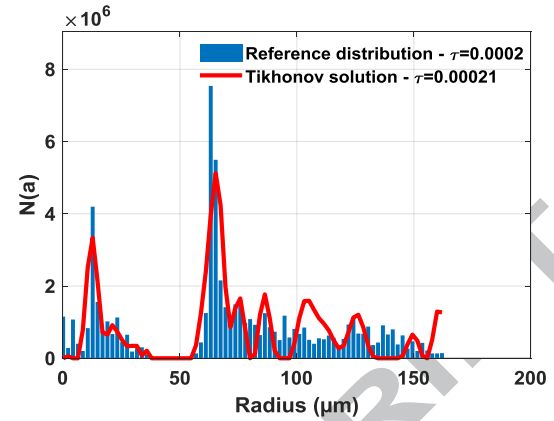

Figure 6: A reference distribution obtained experimentally (blue bars) and the recovered solution (red line) using eq. (9)

This procedure is also relevant for more exotic distributions such as the one shown in Figure 6 which was characterised optically. In this case, the acoustical inversion was not possible because our transducers are inefficient at the low frequencies required to characterise large bubbles ($\geq 110~\mu m$). Nevertheless, the use of synthetic data shows that the inversion procedure remains possible albeit difficult. The L-surface (Figure 7) proposes a maximum radius of 162 μm, which corresponds to the radius of the largest bubble.
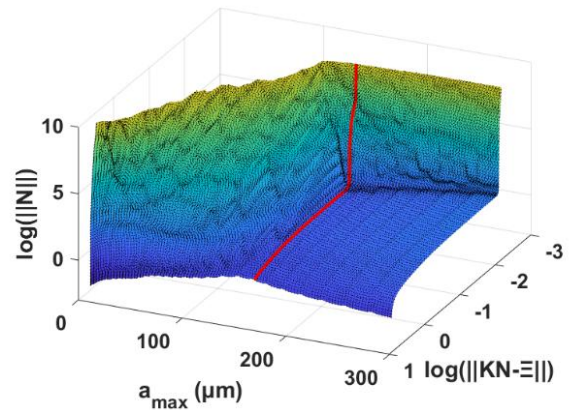
Figure 7: L-surface for a bi-modal experimental bubble size distribution. The red line plots the L-curve with the selected a_{max}.

Hansen shows that when the solution is too smooth, i.e. it is dominated by the first few singulars values, the regularisation parameter corresponding to the L corner fails to correctly estimate the solution. This should not be the case for 'standard' distributions such as those expected in a reactor configuration. The relative error ϵ_λ versus the regularisation parameter is shown in (

Figure 8). It is defined as:

$$\epsilon_\lambda = \frac{|\|N_\lambda\|_2 - \|N_{true}\|_2|}{\|N_{true}\|_2} \tag{11}$$
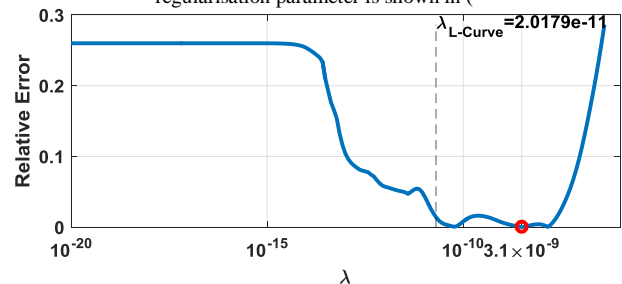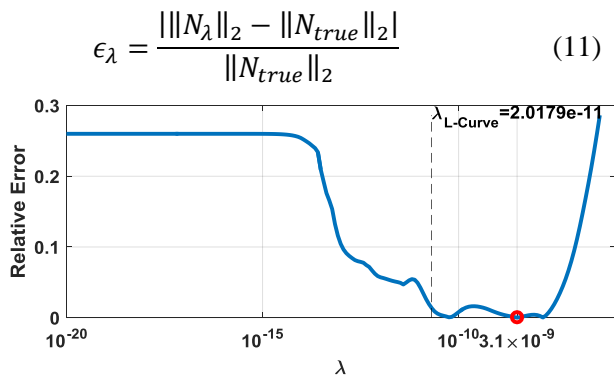

Figure 8: Relative errors for the experimental distribution. The red circle corresponds to the minimum error while the dashed line shows the position of the regularisation parameter selected by the L-curve

This error analysis shows that the regularisation parameter $\lambda_{L-Curve}$ selected by the L-surface does not correspond exactly to the optimal regularisation (which is the one that minimised the relative error). However, the error remains acceptable (around 1%). The main advantage is that the L-surface method provides a robust and systematic way to reach a good regularisation coefficient.

3.2 Experimental bench

Experimentations in liquid sodium should be performed with extreme care as sodium is highly reactive to air and water. Moreover, it is a strong reducing agent which implies using specific transducers designed to operate in such a chemical and thermal environment, e.g. the TUSHT [20]. However, as the acoustical properties of argon bubbles in liquid sodium – especially the impedance contrast – are similar to those of air bubbles in water (see Table 1), preliminary experiments were performed in water.
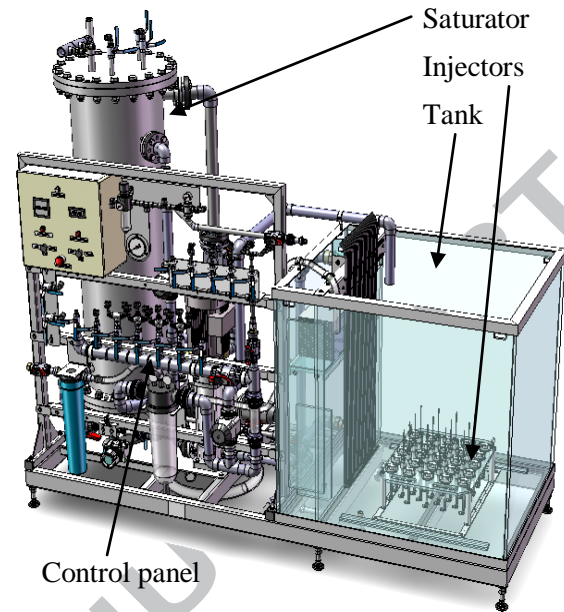
3.2.1 Bubble generation

Figure 9: 3D model of ACWABUL

In order to validate the inversion procedure detailed above, an experimental bench called ACWABUL (Acoustical Characterisation in WAter of BUbbLes) was manufactured at the CEA Cadarache centre to reproduce the required SFR operational conditions in water.

Table 1: Acoustical properties of argon bubbles in liquid sodium compared with those of air bubbles in water [21]–[24]

	UNIT	WATER/AIR 20°C/1 BAR	SODIUM/ARGON 550°C / 1 BAR
Massive thermal capacity of gas	J/(kg.K)	1.01×10^3	520,4
Acoustical velocity in gas	m.s^{-1}	340	535
Acoustical velocity in liquid	m.s^{-1}	1481	2292
Gas compressibility factor	-	0.9996	1.00025
Compressibility of the liquid	Pa^{-1}	4.4×10^{-10}	1.86×10^{-10}
Thermal conductivity of gas	W/(m.K)	0.026	0.0381
Acoustic impedance of gas	rayls	**413**	**311**
Acoustic impedance of liquid	rayls	**1.5×10^6**	**1.9×10^6**
Gas density	Kg.m^{-3}	1.3	0.582
Liquid density	Kg.m^{-3}	1000	816
Surface tension parameter	N.m^{-1}	72.8×10^{-3}	151×10^{-3}
Liquid viscosity	Pa.s	10^{-3}	0.2268×10^{-3}
Acoustical attenuation w/o bubbles	$m^{-1}.Hz^{-2}$	$25 * 10^{-15}$	$12 * 10^{-15}$

This bench consists of a 1m^3 tank, saturator and injectors (Figure 9). Water is first air-saturated at 7 bar in the saturator (300L). It is then injected through specific injectors designed to induce air cavitation (Figure 10) thanks to radial divergence.
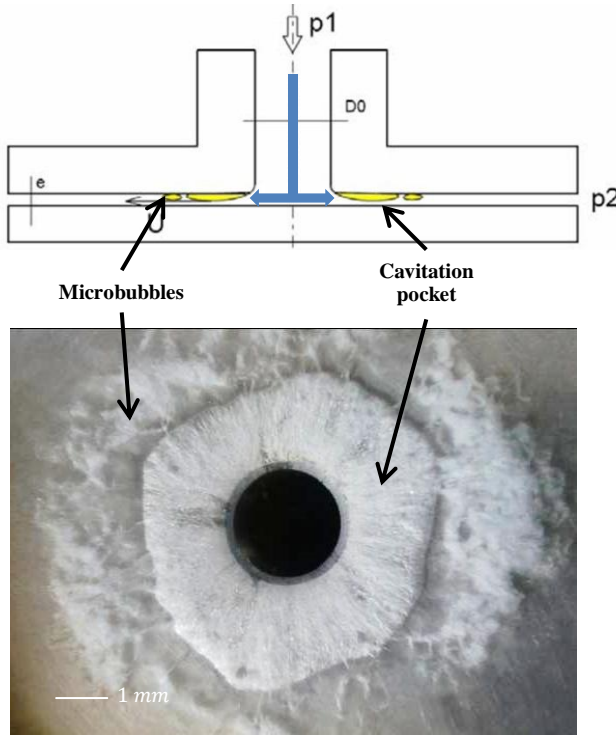
Figure 10: Geometry and image of the microbubble generator (courtesy of Ylec Consultants)

The induced rapid relaxation creates a cavitation pocket which collapses. As the water is over-saturated, stable microbubbles with radii of a few microns to few tens of microns still remain. This process makes it possible to generate clouds like those expected to be found in the reactor.

By varying the numbers of injectors opened and the feeding pump speed rotation, it is possible to adjust the void fraction from $\approx 10^{-7}$ to $\approx 10^{-2}$. The resulting bubbles have a radius between 5 µm and 60 µm with a distribution approximately log-normal.

3.2.2 Acoustic measurements

To estimate the phase velocity and attenuation at every frequency of interest, transmission measurements were performed by sending two sets of $m = 77$ monochromatic 10-cycles bursts. The first set was sent in bubble-free water while the second was sent in bubbly liquid. The bursts ($s_{ref,i}$ and $s_{bubble,i}$) were then compared with each other. The attenuation A_i at the frequency f_i was calculated using (12). The phase velocity V_i at the same frequency was calculated using (13).

$$A_i = \frac{1}{d} \times 20\log\left(\left|\widetilde{s_{bubble,\imath}}(f_i)\right| / \left|\widetilde{s_{ref,\imath}}(f_i)\right|\right) \quad (12)$$

$$\begin{cases} V_i = d / \left(\dfrac{d}{c_{liq}} + \Delta t_i\right) \\ \Delta t_i = \dfrac{\left[\Phi\left(\widetilde{s_{ref,\imath}}(f_i)\right) - \Phi\left(\widetilde{s_{bubble,\imath}}(f_i)\right)\right]}{2\pi f_i} \end{cases} \quad (13)$$

where $\tilde{s} = FFT(s)$ is the fast Fourier transform of the signal s; f_i is the central frequency of the ith burst; d is the distance between the emitter and the receiver; and $\Phi(\tilde{s})$ is the argument of the complex function $\tilde{s}$.
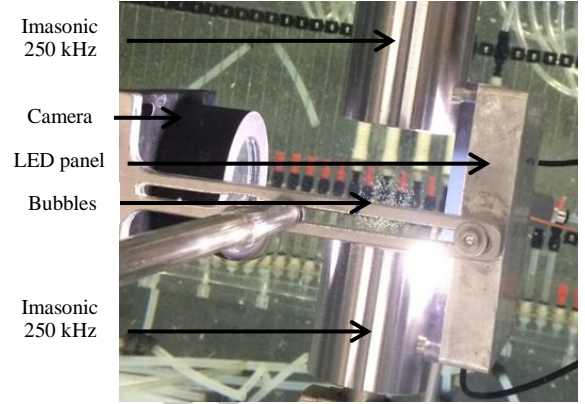

Figure 11: Image of the experimental set-up

To cover the entire frequency range of interest, two custom-made Imasonic® planar transducers (central freq. 250 kHz with an active diameter of 46 mm) were used for broadband measurements between 20 kHz and 400 kHz (Figure 11). The waveforms were generated using a Tektronix® AFG 3022B function generator digitised with a PicoScope® 4824. Both these devices were connected to a computer used to control the experiment through a dedicated Matlab® script. To avoid any non-linearities [25], the wave amplitudes were kept as low as possible.

3.2.3 Optical measurements

A BAUMER® TXG50-IP67 underwater camera with a VS-Technologies® $1,5 \times$ telecentric lens captured several images of the clouds simultaneously with the acoustic measurements. The use of telecentric optics makes it possible to accurately measure the size of a bubble, as its size on the image does not depend on its position in space. However, the depth of field is very narrow, i.e. only few millimetres. Only bubbles with a blurring level below a pre-set level were selected. A dedicated algorithm [2] was then used to estimate the bubble size distribution and the void fraction (Figure 12). The void fraction was determined by measuring the blurring level on each bubble in order to deduce its distance from the focal plane of the camera (Figure 13) using a prior calibration of the optic device. This was used to estimate the volume of interest covered by the camera for each size of bubble.
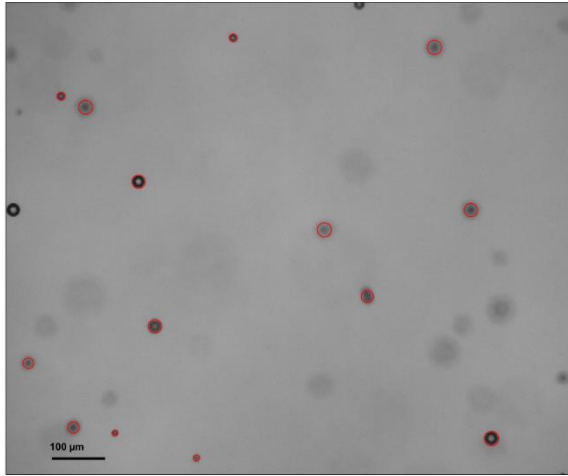
Figure 12: Video frame of the bubble cloud. The bubbles selected and sized are delineated by the red circles

It is worth pointing out that this camera underestimated the number of bubbles with a radius $R_0 \leq 12 \ \mu m$ due to the optics used.
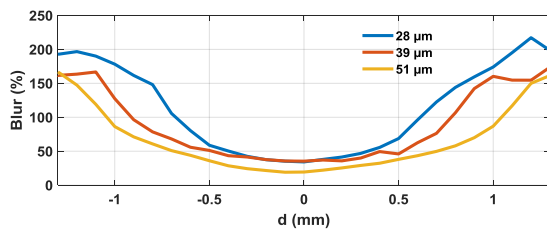

Figure 13: Blur versus distance to the focal plane for different bubbles sizes

Figure 14 shows the void fraction obtained by this optical procedure compared with the one obtained by low-frequency velocity measurements, following the procedure described in another study [19]. The void fraction was modified by switching off a bubble injector at $t = 60 \ s$ and then switching it on again at $t = 120 \ s$.
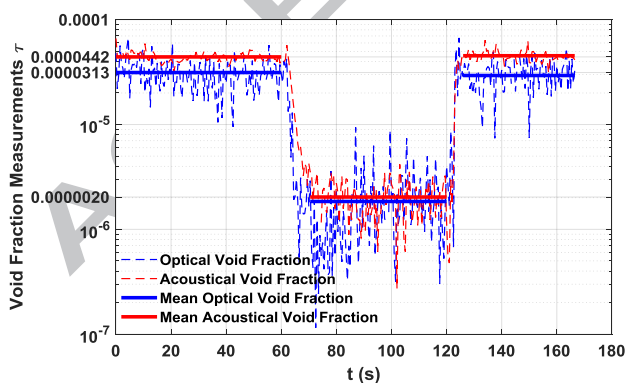

Figure 14: Void fraction estimated by the optical set-up and using sound speed measurements at low-frequency [19]

The optical and acoustic means provided coherent void fraction estimations. There was a small bias between the optical and acoustical estimations. It increased with the void fraction, though remained within the measurement uncertainties. This discrepancy may be due to the fact that the bubbles may become too close to each

other as τ increases and may therefore be rejected by the algorithm as being non-circular. The void fraction measurement by optical means can therefore be considered reliable as long as the cloud volumes seen by the camera and those in which the ultrasound propagates are (spatially) homogeneous.

4 RESULTS AND DISCUSSION

The procedure detailed in paragraph 3.1 was applied to experimental acoustic spectral measurements and the resulting distributions were compared with those obtained optically. The first next paragraph describes the performance of the method for a single histogram, while the second one focuses on the continuous monitoring of the bubble cloud.

4.1 Results for a single cloud

The distribution produced the dispersion curves described in Figure 15. The measurements were performed between $20 \ kHz$ and $400 \ kHz$ using the experimental set-up presented in Figure 11.
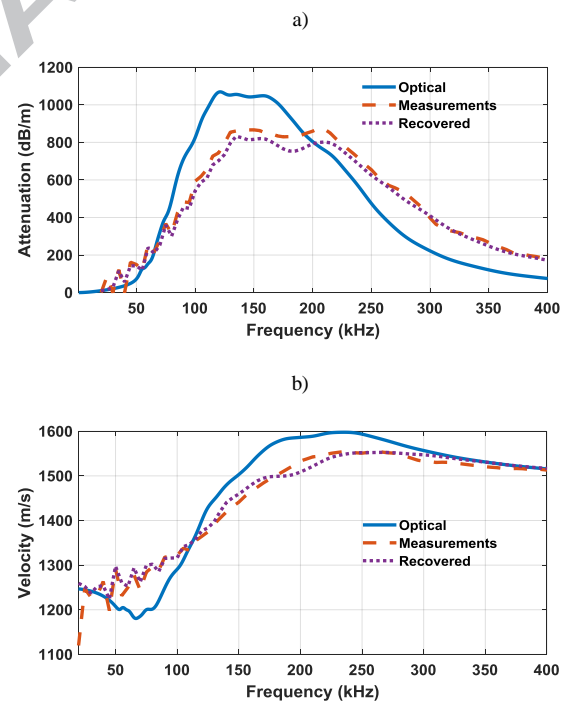

Figure 15: Dispersion curves calculated from the optical measurements (blue line), measured by acoustic means (orange dashed line) and calculated from the recovered distribution (purple dotted line)

The estimation results are shown in Figure 17. The a_{max} selected by the L-surface (Figure 16) is $98 \ \mu m$ and the inversion results are illustrated in Figure 17. This value is greater than the $58 \ \mu m$ obtained previously with simulated data. To overcome the strong attenuation, it is true that the transducers must be close to each other ($5 \ cm$). At low frequencies, the reflections overlap the direct signal and deteriorate the measurements. This explains the oscillations visible in the dispersions

curves (Figure 15) between 20 kHz and 100 kHz, which lead to oscillations in the attenuation and velocity measurements.
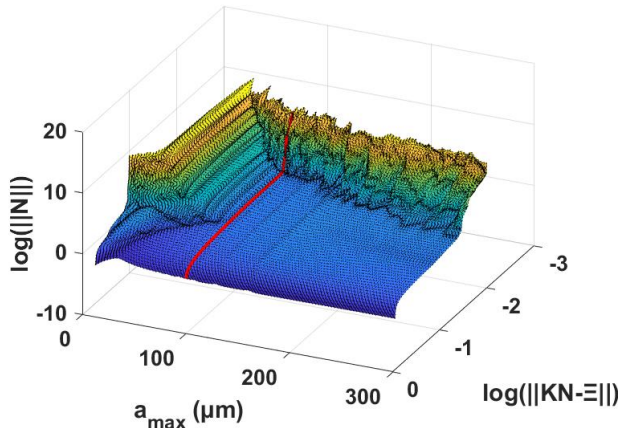

Figure 16: L-surface for the bubble cloud.
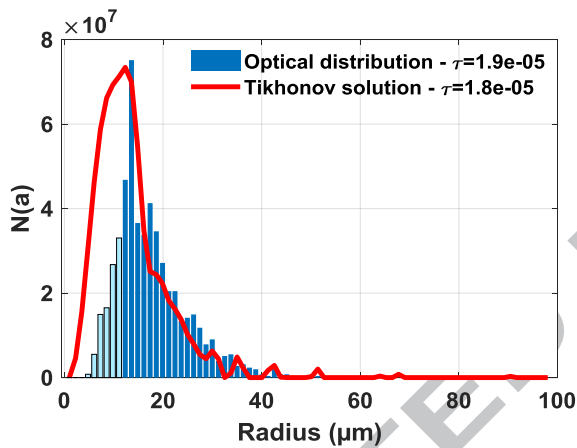The red line plots the L-curve at 98 µm

Figure 17: Inversions results.
$\tau_{optical} = 1.9 * 10^{-5}; \tau_{Tik} = 1.8 * 10^{-5}$.
The light blue bars belong to the domain where the camera cannot correctly estimate the bubble distribution

This situation creates some populations with radii exceeding 58 µm (small peaks after 60 µm, see Figure 17). The void fraction based on the optical data is $\tau_{optical} = 1.9 * 10^{-5}$ whereas the one calculated from the acoustic histogram is $\tau_{Tik} = 1.8 * 10^{-5}$. The distributions are quite similar with a correlation coefficient equal to 0.96. Only bubbles greater than 12 µm were considered since the smallest bubbles were not clearly detected by the optical device. However, as shown by simulation in Figure 5, the inversion method works for all bubble sizes. Moreover, it is can be seen that the estimated histogram presents bin sizes of 1.25 µm. Such a resolution has never been reported before.

4.2   Continuous monitoring

In another experiment, the bubble cloud generation was continually modified by varying the rotating speed of the pump. Regarding the generation method, the bubble creation rate was expected to be related to the rotating speed. Both acoustic and optical data were recorded during half

an hour with one acquisition per minute. For each acquisition, the bubble size distribution was estimated using Tikhonov regularisation and both the void fraction and mean radius were calculated from this histogram and compared with those obtained using optical means (Figure 18 and Figure 19). In order to obtain consistent results between optical and acoustical measurements, only the bubbles larger than 12 µm were considered. During monitoring, the whole inversion procedure was automated using the L-surface method.
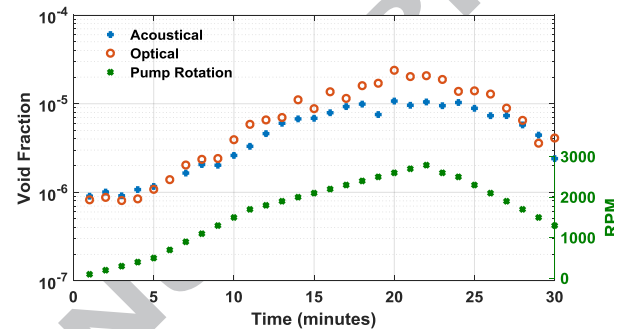

Figure 18: Void fraction monitoring using inverted attenuation and velocity measurements

As expected, it is clear from Figure 18 that both acoustic and optical void fractions follow the pump rotating speed. Acoustic and optical results are in very good agreement, even if a slight saturation effect of the acoustic estimates can be observed at the higher rotating speed.
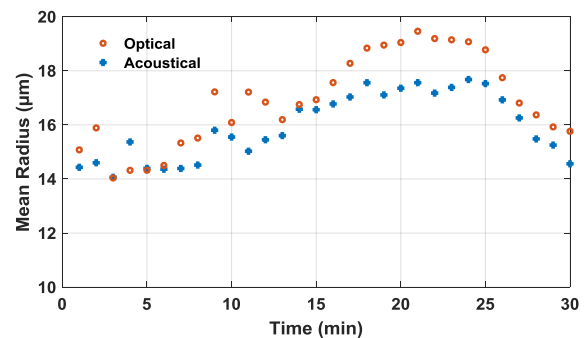
Figure 19: Monitoring the mean radius for bubbles greater than 12 µm

Regarding the mean radius (Figure 19) (here again, only bubbles larger 12 µm were considered), the optical and acoustical mean radii estimated are in general agreement. They are also highly correlated with the rotation speed, which is coherent with the generation principle (Figure 10). Moreover, the bubble size distributions are well determined with an average correlation coefficient of 0.9 without any supervision of the choice of parameters.

4.3   Discussion

While previous studies have attempted to characterise bubble clouds, most of them suffer from a lack of comparison with other means of

characterisation. To our knowledge, only the Dynaflow Laboratory has performed both optical and acoustic characterisations during the development of the Acoustic Bubble Spectrometer$^{©®}$ (ABS) [26] but the resolution is still limited to bin sizes of about 10 µ*m*. Moreover, even if the bubble size distribution has been corroborated by optical means, no cross-evaluations of the void fraction have been provided. With this 10 µm resolution, a correlation coefficient of 0.86 can be estimated from the data found in [26].

The L-surface method used in this study makes it possible to optimise the interval (bubble size) of integration in the inversion formula (Eq. (4)) without providing additional prior information on the size range. Furthermore, the class width can still be reduced insomuch as the spectroscopic measurements are performed with a higher spectral density (i.e. a higher sampling rate). This approach has led to a high correlation coefficient (> 0.95) on the relevant bubble size interval covered by both characterisation procedures and bin sizes of 1.25 µm.

While stabilising the data inversion (Fredholm equation), the automatic regularisation procedure presented here paves the way to real-time monitoring. Though the results of this study are convincing, they are nevertheless subject to optical limitations, especially the smaller bubbles which are poorly counted.

5 CONCLUSION

The bubble cloud characterisation method developed in this paper was performed without requiring prior information on the bubble-size interval. It was achieved using an L-Surface analysis, which provides a systematic method of selecting both the maximum radius of the bubble size interval and Tikonov's regularisation parameter. This procedure was applied to experimental clouds of log-normal size distributions, which are known to be representative of those to be monitored in SFRs. The method also proved efficient in the presence of complex distributions. The results seem to indicate a promising level of efficiency with respect to histogram assessments. The optical comparison resulted in a correlation coefficient over 0.95. Moreover, the present method was successfully applied to continuous bubble cloud monitoring based on the real-time implementation of the modified ultrasonic spectroscopy procedure. This monitoring method is expected to meet the safety requirements for operational SFR conditions. It will be improved to reach full autonomy (self-assessment of the measurement quality) and to

provide automatic alarms in case of anomalies (e.g. deviation from log-normal bubble distribution).

This procedure was evaluated in water. For sodium applications, high-temperature ultrasonic transducers [20] called TUSHT are being developed by the CEA. The possibility of using such specific transducers for void fraction measurements has already been studied by Cavaro [19].

7 REFERENCES

[1] E. Tatsumi, T. Takata, and A. Yamaguchi, "Modeling And Quantification Of Nucleation, Dissolution And Transportation Of Bubbles In Primary Coolant System Of Sodium Fast Reactor," in *The Proceedings of the International Conference on Nuclear Engineering (ICONE)*, Nagoya, Japan, 2007, vol. 2007.

[2] M. Cavaro *et al.*, "Towards in-service acoustic characterization of gaseous microbubbles applied to liquid sodium," in *2009 First International Conference on Advancements in Nuclear Instrumentation Measurement Methods and their Applications (ANIMMA)*, 2009, pp. 1–6.

[3] H. Medwin, "In situ acoustic measurements of bubble populations in coastal ocean waters," *J. Geophys. Res.*, vol. 75, no. 3, pp. 599–611, Jan. 1970.

[4] H. Medwin, "Acoustical determinations of bubble- size spectra," *J. Acoust. Soc. Am.*, vol. 62, no. 4, pp. 1041–1044, Oct. 1977.

[5] J. W. Caruthers, P. A. Elmore, J. C. Novarini, and R. R. Goodman, "An iterative approach for approximating bubble distributions from attenuation measurements," *J. Acoust. Soc. Am.*, vol. 106, no. 1, pp. 185–189, Jul. 1999.

[6] P. A. Elmore and J. W. Caruthers, "Higher order corrections to an iterative approach for approximating bubble distributions from attenuation measurements," *IEEE J. Ocean. Eng.*, vol. 28, no. 1, pp. 117–120, Jan. 2003.

[7] K. Commander and E. Moritz, "Off- resonance contributions to acoustical bubble spectra," *J.*

Acoust. Soc. Am., vol. 85, no. 6, pp. 2665–2669, Jun. 1989.

[8] K. W. Commander and E. Moritz, "Inferring Bubble Populations in the Ocean from Acoustic Measurements," in *OCEANS '89. Proceedings*, 1989, vol. 4, pp. 1181–1185.

[9] R. Duraiswami, "Bubble Density Measurement using an Inverse Acoustic Scattering Technique," *ASME*, vol. 153, pp. 67–73, 1993.

[10] R. Duraiswami, S. Prabhukumar, and G. L. Chahine, "Acoustic measurement of bubble size distributions: Theory and experiments," *J. Acoust. Soc. Am.*, vol. 100, no. 4, p. 2804, 1996.

[11] R. Duraiswami, S. Prabhukumar, and G. L. Chahine, "Bubble counting using an inverse acoustic scattering method," *J. Acoust. Soc. Am.*, vol. 104, no. 5, pp. 2699–2717, Nov. 1998.

[12] X. Wu and G. L. Chahine, "Development of an acoustic instrument for bubble size distribution measurement," *J. Hydrodyn. Ser B*, vol. 22, no. 5, Supplement 1, pp. 330–336, Oct. 2010.

[13] G. L. Chahine and K. M. Kalumuck, "Development of a Near Real-Time Instrument for Nuclei Measurement: The ABS Acoustic Bubble Spectrometer®," pp. 183–191, Jan. 2003.

[14] T. G. Leighton, S. D. Meers, and P. R. White, "Propagation through nonlinear time-dependent bubble clouds and the estimation of bubble populations from measured acoustic characteristics," *Proc. R. Soc. Lond. Math. Phys. Eng. Sci.*, vol. 460, no. 2049, pp. 2521–2550, Sep. 2004.

[15] K. Commander and A. Prosperetti, "Linear Pressure Waves in Bubbly Liquids - Comparison Between Theory and Experiments," *J. Acoust. Soc. Am.*, vol. 85, no. 2, pp. 732–746, Feb. 1989.

[16] K. W. Commander and R. J. McDonald, "Finite- element solution of the inverse problem in bubble swarm acoustics," *J. Acoust. Soc. Am.*, vol. 89, no. 2, pp. 592–597, Feb. 1991.

[17] P. C. Hansen, "The L-Curve and its Use in the Numerical Treatment of Inverse Problems," in *Computational Inverse Problems in Electrocardiology, ed. P. Johnston, Advances in Computational Bioengineering*, 2000, pp. 119–142.

[18] P. C. Hansen, "REGULARIZATION TOOLS: A Matlab package for analysis and solution of discrete ill-posed problems," *Numer. Algorithms*, vol. 6, no. 1, pp. 1–35, 1994.

[19] M. Cavaro, "A Void Fraction Characterisation by Low Frequency Acoustic Velocity Measurements in Microbubble Clouds," *Phys. Procedia*, vol. 70, pp. 496–500, 2015.

[20] C. Lhuillier, B. Marchand, J. M. Augem, J. Sibilo, and J. F. Saillant, "Generation IV nuclear reactors: Under sodium ultrasonic transducers for Inspection and Surveillance," in *2013 3rd International Conference on Advancements in Nuclear Instrumentation, Measurement Methods and their Applications (ANIMMA)*, 2013, pp. 1–6.

[21] J. GIRARD, "PROPRIETES PHYSIQUES DU SODIUM LIQUIDE," CENTRE D'ÉTUDES NUCLÉAIRES DE CADARACHE, Recommandations, 1974.

[22] P. Mouchet and M. Roustan, "Caractéristiques et propriétés des eaux - Eau pure, eaux naturelles," *Tech. Ing.*, 2011.

[23] M. J. Holmes, N. G. Parker, and M. J. W. Povey, "Temperature dependence of bulk viscosity in water using acoustic spectroscopy," *J. Phys. Conf. Ser.*, vol. 269, no. 1, p. 012011, 2011.

[24] E. W. Lemmon and R. T. Jacobsen, "Viscosity and Thermal Conductivity Equations for Nitrogen, Oxygen, Argon, and Air," *Int. J. Thermophys.*, vol. 25, no. 1, pp. 21–69, Jan. 2004.

[25] M. Cavaro, C. Payan, S. Mensah, J. Moysan, and J.-P. Jeannot, "Linear and nonlinear resonant acoustic spectroscopy of micro bubble clouds," *Proc. Meet. Acoust.*, vol. 16, no. 1, p. 045003, Oct. 2012.

[26] Dynaflow, Inc., "ABS Acoustic Bubble Spectrometer | Dynaflow, Inc." [Online]. Available: http://www.dynaflow-inc.com/Products/ABS/Acoustic-Bubble-Spectrometer.htm. [Accessed: 13-Oct-2017].

Highlights

- Acoustical monitoring and characterization of microbubble clouds using Tikhonov regularization
- High resolution bubble size distribution and void fraction values validation by optical means
- Integration domain determination by an original L-Surface analysis